
Benchmarking and Boosting Radiology Report Generation for 3D High-Resolution Medical Images

Che Liu^{1*}, Zhongwei Wan^{2*}, Yuqi Wang³, Hui Shen², Haozhe Wang⁴,
Kangyu Zheng², Mi Zhang², Rossella Arcucci¹

¹ Imperial College London ² The Ohio State University

³ University of Hong Kong

⁴ Hong Kong University of Science and Technology
che.liu21@imperial.ac.uk

Abstract

Automatic radiology report generation can significantly benefit the labor-intensive process of report writing by radiologists, especially for 3D radiographs like CT scans, which are crucial for broad clinical diagnostics yet underexplored compared to 2D radiographs. Existing methods often handle 3D volumes either slice-wise or with aggressive downsampling due to current GPU memory limitations, which results in a loss of the inherent 3D nature and critical details. To overcome these issues, we introduce a novel framework that efficiently and effectively generates radiology reports for high-resolution (HR) 3D volumes, based on large language models (LLMs). Specifically, our framework utilizes low-resolution (LR) visual tokens as queries to mine information from HR tokens, preserving detailed HR information while reducing computational costs by only processing HR informed LR visual queries. Further benefiting the field, we curate and release BIMCV-RG, a new dataset with 5,328 HR 3D volumes and paired reports, establishing the first benchmarks for report generation from 3D HR medical images. Our method consistently surpasses existing methods on this benchmark across three different settings: normal-resolution, high-resolution inputs, and zero-shot domain transfer, all at an acceptable computational cost, trainable on a single A100-80G GPU.

1 Introduction

Radiology reports are essential for clinical decision making, yet their manual creation is labor-intensive and time-consuming [3, 4, 5, 6, 7, 8]. This has necessitated the automation of radiology report generation. Existing work on radiology report generation primarily focuses on 2D images such as chest X-rays [9, 10, 11]. However, compared to 3D images, 2D images offer limited diagnostic information and therefore fall short in identification of some of the most critical and life-threatening diseases such as pulmonary opacities and early-stage cancer [12, 13].

In 3D medical image analysis, high-resolution (HR) images are more clinically informative than their low-resolution (LR) counterparts, as certain diseases, such as pulmonary nodules, are difficult to detect in LR images [14]. Despite the clinical advantages of HR 3D medical images, current studies downsample HR volumes (e.g., $512 \times 512 \times 256$) to LR ($256 \times 256 \times 32$) for radiology report generation with large language models (LLMs) [1, 2]. This results in significant information loss (512 vs. 256 , 256 vs. 32) and could miss lesions that are challenging to detect in LR views. The main reason for downsampling is the increased computational cost when processing the larger number of visual tokens from HR 3D volumes by LLMs, as illustrated in Fig 1 (left). For instance, a standard

* Equal Contribution.

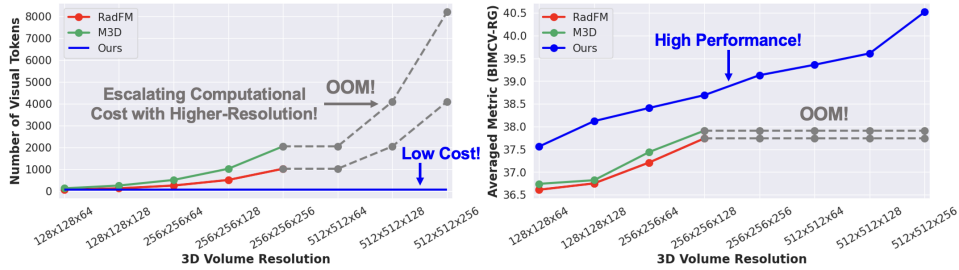


Figure 1: Relationship between the number of visual tokens processed by the LLMs and report generation performance with the BIMCV-RG dataset. **Left:** For RadFM and M3D [1, 2], the number of visual tokens processed by the LLM increases with the input 3D volume resolution. In contrast, our method maintains a constant token count, ensuring computational efficiency. **Right:** Our method consistently improves report generation performance with increasing 3D volume resolution, while competing methods struggle at $256 \times 256 \times 256$ resolutions due to out-of-memory (OOM) from high token counts when batchsize = 1. Refer to Sect 5.2 for details.

CT scan [15] with dimensions of $512 \times 512 \times 256$ generates 4,096 visual tokens, each measuring $32 \times 32 \times 16$. Processing these tokens with common multimodal large language model (MLLM) architectures, such as LLaVA [16] combined with Llama3-8B [17], often leads to out-of-memory (OOM) issues during training on single A100-80GB GPU, as depicted in Fig 1 (right). Another approach involves processing the 3D volume slice-by-slice [18], potentially losing crucial 3D context and consistency along the transverse axis. This leads to a critical challenge: *Can we generate radiology reports for HR 3D medical images using LLMs in a compute-efficient manner while preserving HR information?*

To address this challenge, our work makes three contributions:

- We introduce **High-resolution Informing Low-resolution Tokens (HILT)**, which effectively mines HR information through LR visual queries. This approach allows LLMs to process costs based solely on the number of LR queries instead of the increasing number of HR tokens with higher resolution inputs, while still preserving HR information for enhanced performance, as shown in Fig 1.
- To thoroughly benchmark the **3D High-Resolution Medical Image Report Generation (3DHRG)** task, we curate a new large-scale dataset based on publicly accessible sources, consisting of 5,328 paired HR 3D CT volumes and radiology reports, named BIMCV-RG². This dataset allows the community to assess the generalizability of the 3DHRG task under zero-shot domain transfer scenarios, a significant addition given **there was only one large-scale dataset previously available** for this task.
- We establish the first benchmark for the 3DHRG task across two large datasets and three settings: normal-resolution, high-resolution inputs, and zero-shot domain transfer. Our method consistently achieves superior performance across all the settings for both datasets with a fixed computational cost for LLMs processing visual tokens.

2 Related Works

Multimodal Large Language Models. The development of Multimodal Large Language Models (MLLMs) combines computer vision and natural language processing to enhance visual and linguistic capabilities. This integration is crucial for tasks that require both visual perception and language comprehension. Models like CLIP [19], Flamingo [20], and BLIP [21] have improved the alignment between these modalities by using extensive image-text data samples, resulting in significant performance gains. LLaVA [16] further simplifies this approach by using a basic linear projector for aligning visual features to language space, involving only a few learnable parts and tailored instruction data to fully leverage the model’s strong capabilities. Despite their effectiveness, these approaches focus mainly on 2D images. To explore the underexplored area of 3D medical images, such as CT scans, we extend the LLaVA framework to incorporate our customized 3D vision encoder and HILT. Our aim is to address the challenge of generating radiology reports for 3D medical images.

²This dataset will be released post-acceptance

Radiology Report Generation for 2D Medical Images. Radiology report generation for 2D medical images involves three primary approaches: (1) Template Selection and Generation, which focuses on sentence crafting and differentiating regions using dual writers [22, 23, 24]. (2) Data Integration and Coherence, that integrates knowledge for consistency and highlights abnormal features [25, 26]. (3) Cross-Modal alignment, using attention mechanisms to align textual and visual features and improve semantic accuracy [27, 9, 10]. However, these methods are limited in 2D imaging, such as chest X-rays, and adapting them to 3D medical imaging like CT scans is challenging. This difficulty arises from the inherent differences between the 3D context of volumetric data and 2D multichannel images, as shown in Fig 2 (a). For example, in CT scans, each slice captures unique patterns: upper slices might show the lungs and heart, while lower ones display abdominal organs like the liver, underscoring the unique spatial information in each slice. In contrast, 2D images exhibit only variations in intensity across uniform spatial structures in all channels [28, 29, 30, 31, 32].

Radiology Report Generation for 3D Medical Images. Although 3D medical imaging is crucial for clinical decision making, only a few studies such as CT2Rep [33], RadFM [1], and M3D [2] have explored the task of report generation for such images and provided official code for reimplementations. However, these methods have limitations: as depicted in Fig 2 (b), CT2Rep processes HR 3D volumes slice by slice, sacrificing the 3D context and potentially losing consistency across the transverse axis. In Fig 2 (c), RadFM downsamples HR inputs to LR views, losing critical information from original HR 3D volumes, while M3D not only downsamples HR inputs but also applies spatial pooling to visual tokens, further reducing spatial information. Additionally, all three methods process visual tokens with LLMs for report generation, resulting in increased computational costs as volume resolution increases. Maintaining HR information in medical imaging is crucial, as reducing the coronal and sagittal resolution could corrupt crucial subtle abnormal patterns [12, 13], diminishing the quality of the generated reports. Additionally, clinical practice often prefers 256-slice CT scans over those with fewer slices for their enhanced detail and diagnostic value [34, 35], as downsampling on the transverse axis reduces the model’s ability to capture these 3D patterns, thereby limiting its clinical applicability. In this work, we design a method to generate radiology reports for 3D HR medical images that preserves HR information without downsampling or pooling. This approach keeps **computational costs constant** for processing visual tokens with LLMs, regardless of volume resolution. It consistently outperforms existing methods across resolutions from $128 \times 128 \times 64$ to $512 \times 512 \times 256$, as shown in Figure 1.

3 Generating Radiology Report for HR 3D Medical Images

Our framework is straightforward yet effective: it utilizes a single vision encoder to extract visual embeddings simultaneously from both LR and HR views of a given 3D volume. Subsequently, we introduce **High-resolution Informing Low-resolution Tokens (HILT)**, which treats LR visual tokens as queries and enhances them by integrating mined regional information from all HR visual tokens. Moreover, the LLMs exclusively process HILT for report generation, rather than the entire set of HR visual tokens. This approach ensures efficiency by limiting the computational cost to a constant as the number of LR queries, achieved without resorting to brute-force downsampling and spatial pooling, thereby preserving HR information.

3.1 Unified Processing of LR and HR 3D Volumes Using Single Visual Encoder.

In our framework, the standard ViT [38] serves as the 3D vision encoder, represented by E_V , with a 3D visual tokenizer for tokenizing 3D volume input into patches. This 3D vision encoder optimizes computational efficiency by simultaneously processing both LR and HR views of 3D volumes. As illustrated in Fig 2 (d), the HR 3D volume, denoted as $X^{HR} \in \mathbb{R}^{H \times W \times D}$, where H , W , and D represent the dimensions of height, width, and depth (number of slices), respectively. The LR view is obtained from the HR input volume using bilinear interpolation and is represented as $X^{LR} \in \mathbb{R}^{H' \times W' \times D'}$, where $H' \leq H$, $W' \leq W$, and $D' \leq D$ indicate the reduced dimensions of the LR view. Both HR and LR views are encoded using the same vision encoder. The positional embeddings are initialized based on the dimensions of the HR volume and interpolated to match the LR volume dimensions during the encoding of the LR view. The resulting HR visual embeddings, denoted as $Z^{HR} \in \mathbb{R}^{N \times C}$, where N represents the number of HR visual tokens, and C represents the embedding dimensions. Similarly, the LR visual embeddings are represented as $Z^{LR} \in \mathbb{R}^{N' \times C}$, where N' is the number of LR visual tokens. The visual encoding process is formulated as follows:

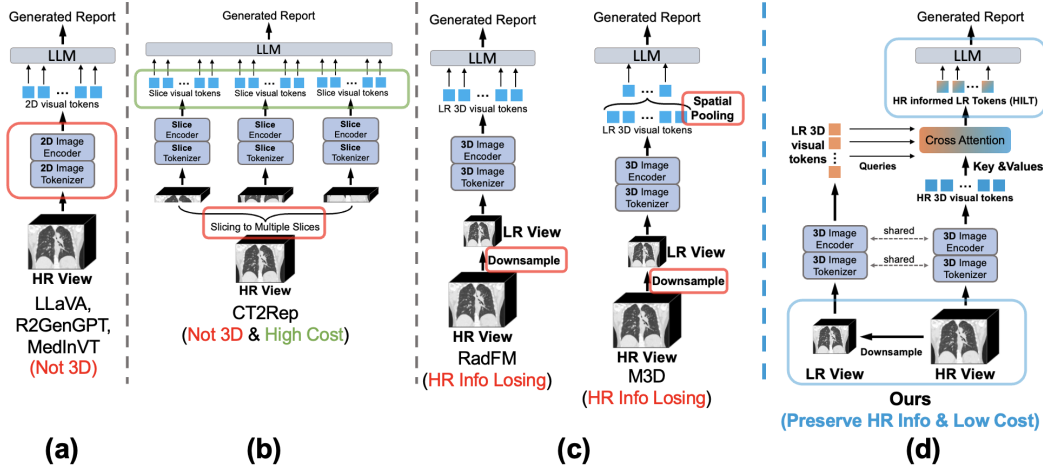


Figure 2: Mainstream radiology report generation methods for 3D medical images using LLMs. We use red and green box to highlight existing deficiencies, and denote our method’s advantages in blue/defrance. We omit text instructions input branch for all methods for simplicity. **(a)**: Methods [16, 36, 37] process 3D volumes as 2D inputs, losing the inherent 3D nature. **(b)**: CT2Rep [18] processes 3D volumes in slice-wise using a shared encoder. The LLM processes all slice visual tokens for generating reports, leading to increased computational costs as the resolution increases. **(c)**: RadFM and M3D [1, 2] downsample 3D HR inputs to LR views, risking loss of critical spatial details. M3D further pools LR visual tokens, reducing spatial information in the latent space. Both methods process all visual tokens with the LLM, increasing computational costs with higher resolutions. **(d)**: Our method simultaneously obtains LR and HR visual tokens with a single vision encoder, using HR tokens to inform LR tokens. This preserves HR detail while only processing LR queries through the LLM, minimizing computational costs.

$$Z^{\text{HR}} = E_V(X^{\text{HR}}), \quad Z^{\text{LR}} = E_V(X^{\text{LR}}) \quad (1)$$

$$Z^{\text{HR}} \in \mathbb{R}^{N \times C}, \quad Z^{\text{LR}} \in \mathbb{R}^{N' \times C} \quad (2)$$

3.2 HILT: High-resolution Informing Low-resolution Tokens.

We utilize the previously generated HR features, Z^{HR} , to enrich LR features, Z^{LR} . This process creates HR-informed LR visual tokens, integrating HR information into LR tokens without corrupting HR spatial information through downsampling or spatial pooling. Specifically, LR visual tokens, Z^{LR} , serve as queries, $Q \in \mathbb{R}^{N' \times C}$. Simultaneously, HR visual tokens, Z^{HR} , act as both keys, $K \in \mathbb{R}^{N \times C}$, and values, $V \in \mathbb{R}^{N \times C}$. This process is depicted in Fig 2 (d). The operation of HR informing LR tokens is mathematically described as:

$$Z^{\text{HILT}} = \mathcal{F}(Q + \text{Softmax}(QK^T)V), \quad Z^{\text{HILT}} \in \mathbb{R}^{N' \times C} \quad (3)$$

Here, \mathcal{F} represents the two-layer projector. We ablate the number of layers of the projector in Sec A.5 and show it in Fig 8.

During this operation, each LR query interacts with all regional HR visual features, preserving these HR features in the relevant LR query. Additionally, we merge the LR queries that have not interacted with HR visual tokens with those that have, ensuring that global information is retained. This prevents the loss of global context from LR queries after interactions with regional HR features. Consequently, Z^{HILT} includes both global and regional features, essential for generating radiology reports that require both comprehensive descriptions and specific regional details. This method compresses a vast number of HR tokens into fewer LR queries, ensuring that the number of visual tokens processed by the LLM is consistent with the number of LR queries, even as the HR input resolution increases. This approach maintains computational efficiency and preserves HR information in Z^{HILT} , allowing us to manage very high-resolution inputs at an acceptable cost. It’s worth noting that we ablate the LR queries by randomly initialized queries, similar to BLIP [21] in Tab 3, and observe a significant performance drop, as illustrated in Sec 5.5.

3.3 Generating Radiology Reports.

We concatenate Z^{HILT} , with input textual instruction tokens Z^{T} for LLMs processing, facilitating auto-regressive report generation, similar to the strategy employed in LLaVA [16]. The Z^{HILT} serve as the visual features in the LLM input, with their count always matching the number of LR queries. This strategy effectively reduces computational costs associated with an increasing number of HR visual tokens, particularly as the resolution of 3D volumes rises, without sacrificing critical HR information from the original HR 3D volumes.

$$\text{Generated Report} = \text{LLM}(\text{concat}(Z^{\text{HILT}}, Z^{\text{T}})) \quad (4)$$

4 Benchmarking Radiology Report Generation on HR 3D Medical Image

4.1 Datasets

CT-RATE³. This dataset consists of 50,188 3D chest CT volumes, each paired with a radiology text report. After filtering out duplicate reports, we obtain 24,284 unique CT volume-report pairs. To create training, validation, and testing sets, we randomly split the data into 70%, 10%, and 20%, respectively. Following previous report generation studies [36], we use only the ‘FINDINGS’ section of the reports for our generation tasks.

BIMCV-RG. As CT-RATE is currently the only large-scale publicly accessible dataset for the 3DHRG task, it is insufficient for establishing a comprehensive benchmark. To better assess generalizability of methods, we curated a new dataset based on the BIMCV [39]. Details of the curation steps are provided in Sec A.3. After data curation, we compiled a dataset named BIMCV-RG⁴, consisting of 5,328 samples, each comprising one HR 3D volume and a unique radiology report. We divided BIMCV-RG into training, validation, and testing subsets, comprising 70%, 10%, and 20% of the data, respectively. Since the dataset does not provide separate ‘FINDINGS’ and ‘IMPRESSIONS’, we use the entire report for all experiments.

4.2 Evaluation Metrics

The evaluation of all methods is conducted using nine metrics: BLEU 1-4 [40], METEOR [41], ROUGE 1-2 and L [42], and CIDEr [43]. It should be noted that the the original BIMCV [39] dataset lacks abnormality annotations for each radiology report, therefore, clinical efficacy [9] are not applicable in the evaluations for this work.

4.3 Baselines on Radiology Report Generation

To our knowledge, no existing benchmark evaluates report generation for 3D HR medical images. Therefore, we select five methods processing HR 3D volumes to establish baselines for **3D High-Resolution Medical Image Report Generation (3DHRG)** tasks. We graphically describe these baselines in Fig 2. For fair and consistent comparison, we utilize Llama3-8B-Instruct [17] as the language decoder for all compared methods.

Baselines Using 2D Inputs:

R2GenGPT [36]. This method extracts visual tokens with a 2D visual encoder, projected into the LLM space for report generation. As the model doesn’t accept 3D inputs, we treat the 3D volume as 2D multi-channel images, modifying only the image tokenizer. Since this work originally designed for chest X-ray images [36], we’ve reimplemented their official code⁵ and training strategy for both datasets in this work.

MedVInT [37]. This method, similar to R2GenGPT, processes 3D inputs as 2D multi-channel images. We adapt the image tokenizer to accommodate 3D inputs, utilizing the publicly available MedVInT-TD checkpoint. Fine-tuning followed procedures outlined in the official code⁶.

Baselines Using 3D Slice Window Inputs:

CT2Rep [18]. This method divides the 3D volume into multiple windows, each containing several

³<https://huggingface.co/datasets/ibrahimhamamci/CT-RATE>

⁴This dataset will be released upon acceptance.

⁵<https://github.com/wang-zhanyu/R2GenGPT>

⁶<https://github.com/xiaoman-zhang/PMC-VQA>

Table 1: Average metrics are computed across nine metrics from Fig 3 for 3DHRG tasks on the CT-RATE and BIMCV-RG datasets, using both normal-resolution and high-resolution settings for input volumes. The best results are highlighted in bold. ‘Number of Visual Tokens’ refers to the quantity of visual tokens processed by LLMs for report generation. ‘OOM’ indicates the method cannot be trained on an 80 GB A100-80G GPU due to out-of-memory issues when batchsize = 1. The light gray color indicates that input 3D volumes are converted to non-3D format to match the configurations of the compared methods.

Methods	3D Volume Input?	Input Image Resolution	Number of Visual Tokens	Large Language Model	CT-RATE Averaged Metric	BIMCV-RG Averaged Metric
<i>Normal-Resolution Setting</i>						
R2GenGPT [36]	✗	256 × 256 × 128	256	Llama3-8B-Instruct	34.16	31.17
MedVInT [37]	✗	256 × 256 × 128	256	Llama3-8B-Instruct	34.31	31.89
CT2Rep [18]	✗	256 × 256 × 128	1066	Llama3-8B-Instruct	37.02	34.14
RadFM [1]	✓	256 × 256 × 128	512	Llama3-8B-Instruct	39.96	37.74
M3D [2]	✓	256 × 256 × 128	1024	Llama3-8B-Instruct	41.59	37.91
HILT(Ours)	✓	256 × 256 × 128	64	Llama3-8B-Instruct	43.83	38.79
<i>High-Resolution Setting</i>						
R2GenGPT [36]	✗	512 × 512 × 256	1024	Llama3-8B-Instruct	42.86	34.08
MedVInT [37]	✗	512 × 512 × 256	1024	Llama3-8B-Instruct	43.13	35.84
CT2Rep [18]	✗	512 × 512 × 256	9408	Llama3-8B-Instruct	OOM	OOM
RadFM [1]	✓	512 × 512 × 256	4096	Llama3-8B-Instruct	OOM	OOM
M3D [2]	✓	512 × 512 × 256	8192	Llama3-8B-Instruct	OOM	OOM
HILT(Ours)	✓	512 × 512 × 256	64	Llama3-8B-Instruct	46.05	40.96

slices. The visual encoder processes each window sequentially and concatenates all slice visual tokens for input to the language decoders, which generate the report. While capable of accepting 3D input, it still processes the entire volume slice-wise, potentially compromising its 3D nature and introducing inconsistent artifacts. For fair comparison, we adopted the official code ⁷.

Baselines Using 3D Volume Inputs:

RadFM [1]. This method is able to process 3D volume inputs but is restricted to downsampled versions of original HR 3D medical images, as explained in their original publication [1]. They directly process all 3D visual tokens with LLM to generate radiology reports, incurring high computational costs as the number of tokens increases with HR volume inputs. We utilize their released checkpoints ⁸ for the 3D vision encoder for fair comparison with the original work.

M3D [2]. M3D is a MLLM designed to process HR 3D volumes, utilizing downsampling at the input level and learnable spatial pooling at the latent level to decrease computational demands [2]. However, the use of small patch sizes introduces heavy computational costs due to the large number of visual tokens. We reimplement their approach on CT-RATE and BIMCV-RG datasets using their official code ⁹.

5 Experiments and Evaluation

5.1 Implementation Details.

We utilize the standard ViT-Base architecture for our 3D vision encoder, training it from scratch with a patch size of 32 × 32 × 16. We fixed the LR input size to 128 × 128 × 64 to minimize computational costs. Additionally, we conduct ablation experiments on the LR input resolution, as shown in Tab 4 and discussed further in Sec A.5. The language decoder employed is Llama3-8B-Instruct [17]. Ablation studies on both the ViT and LLM at various scales are detailed in Sec 5.5. For different LLMs, ablation results are specifically discussed in Sec A.5. The details of training are detailed in Sec A.6 and listed in Tab 5. For data preprocessing, we detail our strategy in Sec A.4, applying the same processing techniques across all methods for a fair comparison. An exception is made for methods based on 2D inputs; here, we convert the 3D volumes to 2D multichannel images to accommodate volume inputs.

5.2 Main Results

Normal Resolution. In Tab 1, our method is compared with existing approaches across both normal and high-resolution settings, as well as 2D and 3D input formats. Notably, LR queries derived from

⁷<https://github.com/ibrahimethemhamamci/CT2Rep>

⁸<https://github.com/chaoyi-wu/RadFM>

⁹<https://github.com/BAAI-DCAI/M3D>

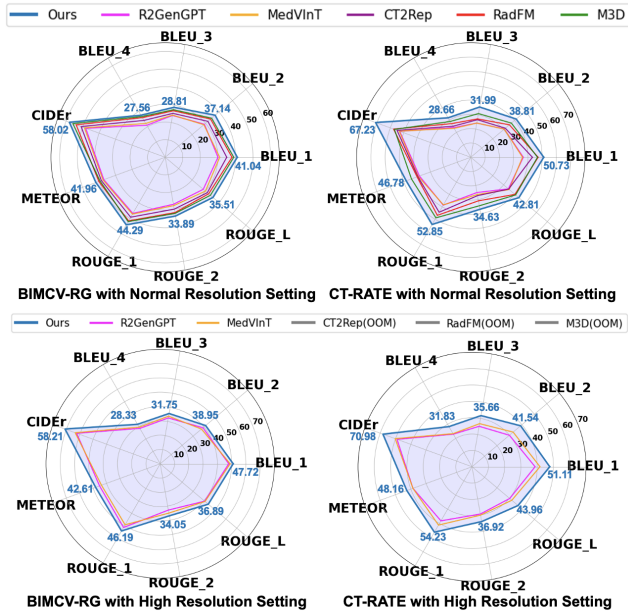


Figure 3: Results of 3DHRG tasks on BIMCV-RG and CT-RATE datasets are evaluated using nine metrics mentioned in Sec 4.2. ‘OOM’ indicates that the method cannot be trained at the setting on a single A100-80G GPU when batchsize = 1. **Top:** Methods with an input resolution of $256 \times 256 \times 128$. **Bottom:** Methods with an input resolution of $512 \times 512 \times 256$.

Methods	CT-RATE \rightarrow BIMCV-RG Averaged Metric	BIMCV-RG \rightarrow CT-RATE Averaged Metric
R2GenGPT [36]	30.26	32.64
MedVInT [37]	30.19	32.89
CT2Rep [18]	32.73	35.14
RadFM [1]	33.91	35.92
M3D [2]	34.22	36.34
HILT(Ours)	36.54	40.21

Table 2: Results of the 3DHRG task under zero-shot domain transfer scenario. Reported results represent the average of nine metrics described in Sec 4.2. ‘CT-RATE \rightarrow BIMCV-RG’ indicates training on CT-RATE and testing on BIMCV-RG, and vice versa. Best results are highlighted in bold.

an LR view of the 3D volume, which has dimensions of $128 \times 128 \times 64$, result in 64 LR queries for generating Z^{HILT} . The averaged metric across nine metrics described in Sec 4.2 is reported in Tab 1, with detailed comparisons for the CT-RATE and BIMCV-RG datasets displayed in Fig. 3 top panel. This highlights our method’s consistent superiority over existing methods across all metrics. From the efficiency aspect, the LLM in our method processes only 64 tokens from HILT for report generation, significantly fewer than those handled by the compared approaches, underscoring the superior performance achieved with fewer visual tokens and highlighting the effectiveness of our method in both efficacy and efficiency.

Existing methods using 3D input outperform those using non-3D input, suggesting the necessity of 3D input for 3DHRG tasks. 2D input methods process fewer tokens but sacrifice the inherent 3D nature of the volume, leading to sub-optimal performance. Hence, preserving 3D context is crucial for better performance in 3DHRG tasks.

High Resolution. As suggested by clinical standards [12, 13, 35], HR 3D medical images provide richer information compared to lower variants. Thus, we increase the input volume resolution from $256 \times 256 \times 128$ to $512 \times 512 \times 256$. However, this increase in volume resolution leads to a higher number of visual tokens processed by LLMs in existing methods, resulting in **OOM** issues for CT2Rep, RadFM, and M3D [33, 1, 2], rendering them untrainable on a single A100-80GB GPU following their official configurations. Only 2D input-based methods are available under HR settings.

Despite the increased resolution of the input volume, our method maintains a constant number of visual tokens processed by the LLM, set at 64 as the number of LR queries. In our method, LLM only processes the HILT rather than all HR visual tokens, ensuring computational efficiency. Our method reaches *the highest* performance across all metrics as depicted in Fig 3 bottom panel, and with *the lowest* cost from the number of LLM processing visual tokens, as shown in Tab 1 HR setting. Demonstrating its effectiveness in handling HR 3D medical images for 3DHRG tasks.

5.3 Zero-shot Domain Transferring

To establish a comprehensive benchmark for 3DHRG, we explore an extreme scenario: zero-shot domain transfer. In this setup, models are trained on one dataset and tested on another, simulating real clinical applications where test data distribution is typically unknown and differs from the training

<p>Single CT technique of pulmonary arteries and p1lob-CT of lower limbs up to the popliteal region.</p> <p>No filling defects are observed in the main, lobar, or segmental pulmonary arteries, without being able to rule out involvement by a more distal level.</p> <p>Small ground-glass opacities are observed in the posterior segment of both upper lobes as well as some consolidated areas in the right lower lobe with a posterior predominance, small focus of consolidation in the posterior segment of the left lower lobe.</p> <p>Findings related to a mild to moderate COVID pneumonia infection.</p> <p>No mediastinal, hilar, or axillary lymphadenopathy of significant size was observed.</p> <p>Absence of pleural and pericardial effusion.</p> <p>Regenerative bone signs in the axial skeleton.</p> <p>Marked degenerative changes.</p> <p>None extending the vascular structures of the lower limbs included in the study, no filling defects suggestive of DVT were seen. Thrombus was observed.</p> <p>Ground Truth</p>	<p>Chest CT, without contrast urgent right basal consolidation with peribronchial extension not suggestive of pulmonary involvement by COVID.</p> <p>No other consolidations or ground-glass opacities are seen.</p> <p>No suspicious pulmonary nodules.</p> <p>Mild bilateral pleural effusion with a right predominance.</p> <p>Dilation of the pulmonary artery trunk presenting a transverse axis of 58-55mm.</p> <p>Cardiac silhouette at the upper limit of normal.</p> <p>No pericardial effusion is seen.</p> <p>Port-a-cath with distal end in SVC. In the first abdominal cuts included in the study, only the presence of abundant intestinal gas and dried feces is noteworthy.</p> <p>Marked degenerative changes in the axial skeleton.</p> <p>Conclusion Right basal consolidation not suggestive of pulmonary involvement by SARS-CoV-2.</p> <p>Mild bilateral pleural effusion.</p> <p>RadFM</p>	<p>A chest CT, without intravenous contrast was performed.</p> <p>No mediastinal or axillary lymphadenopathy was visualized.</p> <p>In the pulmonary parenchyma, the presence of a fibrosing interstitial pattern stands out, with the presence of traction bronchiectasis, which shows a clear predominance in the posterobasal areas of both lungs and is notable for associating dendriform calcifications located both at the subpleural level and affecting the small airway with a budding tree distribution.</p> <p>No honeycombing areas are visualized.</p> <p>Associated with these interstitial changes, some small ground-glass opacities are visualized, which, although they seem to be related to the same, cannot be completely ruled out that they correspond to COVID-19 involvement since they are indistinguishable.</p> <p>There is no pleural or pericardial effusion.</p> <p>No other significant findings.</p> <p>M3D</p>	<p>CT angiography of pulmonary arteries and venous of lower limbs.</p> <p>Main, lobar, and segmental pulmonary arteries are with no evident filling defects.</p> <p>No axillary, mediastinal, or hilar lymphadenopathy of significant size was observed.</p> <p>Persistence of thickened fibrotic tracts, bilateral peripheral laminar atelectasis, and faint ground-glass opacities in all lobes.</p> <p>Cardiomally without significant pericardial effusion.</p> <p>A small, millimetric calcified nodule in the lateral basal segment of the left lower lobe, already known and unchanged, is noted.</p> <p>No suspicious lymphadenopathy of significant size was observed in the thorax.</p> <p>Consolidations with multilobar involvement are observed in the current epidemiological context, is compatible with viral pneumonia due to COVID-19.</p> <p>Absence of pleural and pericardial effusion.</p> <p>Marked degenerative changes in the axial skeleton.</p> <p>Ours</p>	<p>CT angiography of the pulmonary arteries and lower limb venography up to the popliteal region.</p> <p>No evidence of pulmonary thromboembolism is seen in the main, lobar, or segmental pulmonary arteries, although distal involvement cannot be excluded.</p> <p>The mediastinal, hilar, and axillary lymph nodes do not show any significant enlargement.</p> <p>Subtle ground-glass opacities in both upper lobes.</p> <p>Multilobar consolidations are present, which are consistent with viral pneumonia in the context of the current epidemiological situation, likely due to COVID-19.</p> <p>There are no indications of pleural or pericardial effusions.</p> <p>Central airway of normal appearance.</p> <p>Degenerative changes are observed in the axial skeleton.</p> <p>The study is completed with the vascular structures of the lower limbs included in the study, no evident signs of DVT are observed.</p> <p>Ours (HR)</p>
---	---	---	---	---

Figure 4: Qualitative comparison between ground truth and reports generated by existing methods and ours. Blue indicates imaging technology. Green indicates normal information. Brown indicates abnormality. Red highlights incorrect content. Except for the ‘HR’ setting, methods process inputs at normal resolution, as shown in Tab 1. ‘HR’ denotes high-resolution input.

set. We utilize CT-RATE and our proposed dataset BIMCV-RG for this benchmark. These datasets are sourced from distinct populations (Turkish vs. Spanish) and settings (single center vs. multiple centers), underlining the challenge of this scenario and the significance of BIMCV-RG. Previously, only the CT-RATE dataset was available for 3DHRG, limiting the feasibility of zero-shot domain transfer. Tab 2 presents the results for all baseline methods under this scenario. We restrict the input resolutions to $256 \times 256 \times 128$ due to OOM issues encountered by CT2Rep [18], RadFM [1], and M3D [2] with higher resolutions. Our method consistently outperforms all existing methods under the zero-shot domain transfer scenario across both datasets, showcasing the robustness and generalizability of our approach.

5.4 Visualization of Qualitative Results

In Fig 4, we present generated reports alongside ground truth from BIMCV-RG, focusing on three aspects: (1) imaging technology, (2) normal patterns, and (3) abnormal patterns. In RadFM [1] and M3D [2], both methods concentrate solely on the CT modality, neglecting other imaging details and providing very few accurate normal and abnormal contents, often leading to incorrect interpretations. For instance, RadFM incorrectly mentions ‘pleural effusion’, ‘no other consolidation’, and ‘not suggestive of COVID’, despite the ground truth indicating the opposite. Similarly, M3D struggles to identify COVID-19, disregarding clear indications from the ground truth, while also disregarding most normal and abnormal pattern information, resulting in irrelevant content. These deficiencies arise from downsampling and spatial pooling strategies that compromise crucial spatial information from the 3D medical images.

In contrast, our method produces accurate and detailed content, such as ‘CT angiography of pulmonary arteries and veins of the lower limbs,’ accurately capturing imaging technology. Our method also correctly identifies normal and abnormal patterns, for instance, ‘without pericardial effusion’ and ‘faint ground-glass opacities.’ As input resolution increases, our method captures subtler information, like ‘venography up to the popliteal region,’ specifying the CT scan area. ‘Central airway of normal appearance’ suggests subtle regional pathology patterns, which are hard to observe in lower resolution input. Similarly, ‘Subtle ground-glass opacities in both upper lobes’ pinpoint abnormality and location, benefiting from HR input. These findings highlight our method’s superior capability to generate precise and comprehensive radiology reports from 3D medical images compared to existing approaches at normal resolution setting. Additionally, our method enhances report quality in high-resolution setting, contrasting with existing methods encountering OOM issues.

5.5 Analysis

In this section, we evaluate various components, input resolutions, and scales of vision and language models. All ablation studies use five unique random seeds, and we report averages and standard deviations across five runs for nine metrics, as detailed in Sec 4.2.

Ablation Studies on Each Components. In Tab 3, we set LLaVA-1.5 [16] as our baseline, as our method builds upon its architecture. Across both resolution settings, variants with 3D

Table 3: Results of ablation studies with each component. The baseline model, LLaVA-1.5 [16], processes 3D input by converting 3D volume to 2D images, with the transverse axis as the channel axis. ‘3D Vision Encoder’ indicates directly processing input as a 3D volume. ‘Rand. Init. Queries’ indicates using randomly initialized queries to compress HR visual tokens following BLIP [21] strategy. ‘HILT’ indicates our method uses LR queries to mine HR information and compress HR visual tokens. ‘Number of Visual Tokens’ represents the number of visual tokens processed by LLMs. ‘-’ indicates no LR input in this setting. Best results are in bold.

Methods	Input Image (HR)	Input Image (LR)	Number of Visual Tokens	CT-RATE Averaged Metric	BIMCV-RG Averaged Metric
<i>Normal-Resolution Setting</i>					
Baseline (LLaVA-1.5)	$256 \times 256 \times 128$	-	256	33.42	30.76
+3D Vision Encoder	$256 \times 256 \times 128$	-	512	36.52	35.19
+Rand. Init. Queries	$256 \times 256 \times 128$	-	64	36.23	34.79
+HILT (Ours)	$256 \times 256 \times 128$	$128 \times 128 \times 64$	64	43.83	38.69
<i>High Resolution Setting</i>					
Baseline (LLaVA-1.5)	$512 \times 512 \times 256$	-	1024	35.63	33.17
+3D Vision Encoder	$512 \times 512 \times 256$	-	4096	OOM	OOM
+Rand. Init. Queries	$512 \times 512 \times 256$	-	64	41.14	36.21
+HILT (Ours)	$512 \times 512 \times 256$	$128 \times 128 \times 64$	64	46.05	40.96

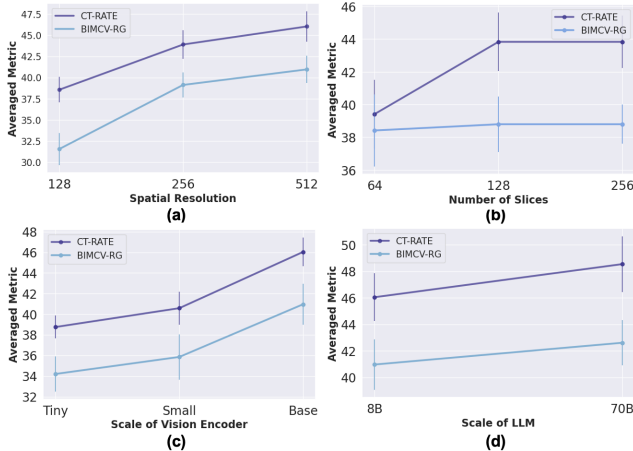


Figure 5: Results of ablation studies across various factors: (a): Averaged metrics for both datasets, varying spatial resolution (sagittal and coronal axes) from 128×128 to 512×512 , with a fixed number of 256 slices. (b): Averaged metrics for both datasets with various number of slices and a fixed spatial resolution of 256×256 . (c): Averaged metrics for both datasets using different scales of 3D vision encoders. (d): Averaged metrics for both datasets using various scales of LLMs, limited to 8B and 70B scales provided by Llama3 [17].

input consistently outperform baselines, highlighting the necessity of 3D context in 3DHRG tasks. While compressing the number of HR visual tokens with randomly initialized queries can reduce computational costs, it leads to poorer performance, even falling short of directly processing all HR visual tokens under normal-resolution settings. Our method, HILT, utilizing LR queries to compress HR visual tokens, significantly outperforms variants using randomly initialized queries in both resolution settings. This can be attributed to each LR query indicating a specific region in the 3D volume and interacting with all regional HR features, thereby preserving HR information in LR tokens along with spatial relations. Conversely, randomly initialized queries lose spatial information from the HR volume, as they do not reflect any spatial relation to the original 3D volumes.

Affect of Resolution of 3D Medical Image. We analyze the impact of varying spatial resolutions along the sagittal and coronal axes, as well as the number of slices along the transverse axis, as shown in Fig 5 (a) and (b). We find that increased resolution across all three axes enhances the 3DHRG task, demonstrating the benefits of HR 3D volumes for radiology report generation. With our efficient method, we can handle HR input at an acceptable cost while preserving HR information.

Scalability Analysis. We evaluate the scalability of our method on vision and language models in Fig 5 (c) and (d), respectively. For the vision encoder, we employ three scales: ViT-Tiny, ViT-Small, and ViT-Base [38]. Regarding language models, we scale from 8B to 70B, as Llama3-Instruct [17] offers versions only in these sizes. Notably, when training with the 80B version, we utilize QLoRA [44] with int4 precision due to hardware limitations. As depicted in Fig 5 (c) and (d), our method consistently improves in performance with both vision and language model scaling. This indicates the scalability of our model and the potential effectiveness of large-scale models for the 3DHRG task.

6 Conclusion

In this work, we introduce a framework for generating radiology reports from HR 3D medical images, maintaining acceptable costs while preserving HR details. At the central of our approach is the **High-resolution Informing Low-resolution Tokens (HILT)**, which integrates HR information into LR queries, enhancing efficiency and effectiveness for handling 3D volumes up to $512 \times 512 \times 256$. We

establish the first benchmark for the 3DHRG task, compare it with existing methods, and introduce the BIMCV-RG dataset for comprehensive benchmarking across three settings: normal and high-resolution inputs, and zero-shot domain transfer. Thanks to HILT, our method demonstrates superior performance on two datasets in these settings at an acceptable cost. We anticipate that our benchmarks and dataset will significantly advance the field of radiology report generation for 3D medical images.

References

- [1] C. Wu, X. Zhang, Y. Zhang, Y. Wang, and W. Xie, "Towards generalist foundation model for radiology," *arXiv preprint arXiv:2308.02463*, 2023.
- [2] F. Bai, Y. Du, T. Huang, M. Q.-H. Meng, and B. Zhao, "M3d: Advancing 3d medical image analysis with multi-modal large language models," *arXiv preprint arXiv:2404.00578*, 2024.
- [3] S. Bastawrous and B. Carney, "Improving patient safety: avoiding unread imaging exams in the national va enterprise electronic health record," *Journal of digital imaging*, vol. 30, pp. 309–313, 2017.
- [4] A. Rimmer, "Radiologist shortage leaves patient care at risk, warns royal college," *BMJ: British Medical Journal (Online)*, vol. 359, 2017.
- [5] A. B. Rosenkrantz, D. R. Hughes, and R. Duszak Jr, "The us radiologist workforce: an analysis of temporal and geographic variation by using large national datasets," *Radiology*, vol. 279, no. 1, pp. 175–184, 2016.
- [6] Z. Wan, C. Liu, X. Wang, C. Tao, H. Shen, Z. Peng, J. Fu, R. Arcucci, H. Yao, and M. Zhang, "Electrocardiogram instruction tuning for report generation," *arXiv preprint arXiv:2403.04945*, 2024.
- [7] Y. Chen, C. Liu, X. Liu, R. Arcucci, and Z. Xiong, "Bimcv-r: A landmark dataset for 3d ct text-image retrieval," *arXiv preprint arXiv:2403.15992*, 2024.
- [8] C. Liu, Z. Wan, C. Ouyang, A. Shah, W. Bai, and R. Arcucci, "Zero-shot ecg classification with multimodal learning and test-time clinical knowledge enhancement," *arXiv preprint arXiv:2403.06659*, 2024.
- [9] T. Tanida, P. Müller, G. Kaissis, and D. Rueckert, "Interactive and explainable region-guided radiology report generation," in *Proceedings of the IEEE/CVF Conference on Computer Vision and Pattern Recognition*, 2023, pp. 7433–7442.
- [10] Y. Li, B. Yang, X. Cheng, Z. Zhu, H. Li, and Y. Zou, "Unify, align and refine: Multi-level semantic alignment for radiology report generation," in *Proceedings of the IEEE/CVF International Conference on Computer Vision*, 2023, pp. 2863–2874.
- [11] Z. Wan, C. Liu, M. Zhang, J. Fu, B. Wang, S. Cheng, L. Ma, C. Quilodrán-Casas, and R. Arcucci, "Med-unic: Unifying cross-lingual medical vision-language pre-training by diminishing bias," *arXiv preprint arXiv:2305.19894*, 2023.
- [12] S. H. Bradley, S. Abraham, M. E. Callister, A. Grice, W. T. Hamilton, R. R. Lopez, B. Shinkins, and R. D. Neal, "Sensitivity of chest x-ray for detecting lung cancer in people presenting with symptoms: a systematic review," *British Journal of General Practice*, vol. 69, no. 689, pp. e827–e835, 2019.
- [13] W. H. Self, D. M. Courtney, C. D. McNaughton, R. G. Wunderink, and J. A. Kline, "High discordance of chest x-ray and computed tomography for detection of pulmonary opacities in ed patients: implications for diagnosing pneumonia," *The American journal of emergency medicine*, vol. 31, no. 2, pp. 401–405, 2013.
- [14] S. Liu, H. Liu, P. Li, and L. Jiang, "Application of high-resolution ct images information in complicated infection of lung tumors," *Journal of Infection and Public Health*, vol. 14, no. 3, pp. 418–422, 2021.
- [15] M. Singh and H. Singh, "Computer assisted imaging for nodule detection on a multi-slice ct image," in *World Congress on Medical Physics and Biomedical Engineering, September 7-12, 2009, Munich, Germany: Vol. 25/5 Information and Communication in Medicine, Telemedicine and e-Health*. Springer, 2009, pp. 301–304.
- [16] H. Liu, C. Li, Q. Wu, and Y. J. Lee, "Visual instruction tuning," *arXiv preprint arXiv:2304.08485*, 2023.
- [17] AI@Meta, "Llama 3 model card," 2024. [Online]. Available: https://github.com/meta-llama/llama3/blob/main/MODEL_CARD.md
- [18] I. E. Hamamci, S. Er, and B. Menze, "Ct2rep: Automated radiology report generation for 3d medical imaging," *arXiv preprint arXiv:2403.06801*, 2024.
- [19] A. Radford, J. Wu, R. Child, D. Luan, D. Amodei, I. Sutskever *et al.*, "Language models are unsupervised multitask learners," *OpenAI blog*, vol. 1, no. 8, p. 9, 2019.
- [20] J.-B. Alayrac, J. Donahue, P. Luc, A. Miech, I. Barr, Y. Hasson, K. Lenc, A. Mensch, K. Millican, M. Reynolds *et al.*, "Flamingo: a visual language model for few-shot learning," *Advances in Neural Information Processing Systems*, vol. 35, pp. 23 716–23 736, 2022.
- [21] J. Li, D. Li, S. Savarese, and S. Hoi, "Blip-2: Bootstrapping language-image pre-training with frozen image encoders and large language models," *arXiv preprint arXiv:2301.12597*, 2023.
- [22] Y. Li, X. Liang, Z. Hu, and E. P. Xing, "Hybrid retrieval-generation reinforced agent for medical image report generation," *Advances in neural information processing systems*, vol. 31, 2018.
- [23] B. Jing, P. Xie, and E. Xing, "On the automatic generation of medical imaging reports," *arXiv preprint arXiv:1711.08195*, 2017.

- [24] Z. Wan, X. Wang, C. Liu, S. Alam, Y. Zheng, J. Liu, Z. Qu, S. Yan, Y. Zhu, Q. Zhang, M. Chowdhury, and M. Zhang, “Efficient large language models: A survey,” 2023.
- [25] F. Liu, X. Wu, S. Ge, W. Fan, and Y. Zou, “Exploring and distilling posterior and prior knowledge for radiology report generation,” in *Proceedings of the IEEE/CVF conference on computer vision and pattern recognition*, 2021, pp. 13 753–13 762.
- [26] X. Ma, F. Liu, C. Yin, X. Wu, S. Ge, Y. Zou, P. Zhang, and X. Sun, “Contrastive attention for automatic chest x-ray report generation,” *arXiv preprint arXiv:2106.06965*, 2021.
- [27] T. Gu, D. Liu, Z. Li, and W. Cai, “Complex organ mask guided radiology report generation,” in *Proceedings of the IEEE/CVF Winter Conference on Applications of Computer Vision*, 2024, pp. 7995–8004.
- [28] A. A. Adegun, S. Viriri, and R. O. Ogundokun, “Deep learning approach for medical image analysis,” *Computational Intelligence and Neuroscience*, vol. 2021, pp. 1–9, 2021.
- [29] M. Puttagunta and S. Ravi, “Medical image analysis based on deep learning approach,” *Multimedia tools and applications*, vol. 80, no. 16, pp. 24 365–24 398, 2021.
- [30] X.-H. Shen, B.-Y. Su, J.-J. Liu, G.-M. Zhang, H.-D. Xue, Z.-Y. Jin, S. A. Mirjalili, and C. Ma, “A reappraisal of adult thoracic and abdominal surface anatomy via ct scan in chinese population,” *Clinical anatomy*, vol. 29, no. 2, pp. 165–174, 2016.
- [31] J. Ker, L. Wang, J. Rao, and T. Lim, “Deep learning applications in medical image analysis,” *Ieee Access*, vol. 6, pp. 9375–9389, 2017.
- [32] S. P. Singh, L. Wang, S. Gupta, H. Goli, P. Padmanabhan, and B. Gulyás, “3d deep learning on medical images: a review,” *Sensors*, vol. 20, no. 18, p. 5097, 2020.
- [33] I. E. Hamamci, S. Er, and B. Menze, “Ct2rep: Automated radiology report generation for 3d medical imaging,” *arXiv preprint arXiv:2403.06801*, 2024.
- [34] O. Klass, M. Walker, A. Siebach, T. Stuber, S. Feuerlein, M. Juchems, and M. H. Hoffmann, “Prospectively gated axial ct coronary angiography: comparison of image quality and effective radiation dose between 64-and 256-slice ct,” *European radiology*, vol. 20, pp. 1124–1131, 2010.
- [35] S.-K. Chua, H.-F. Hung, J.-J. Cheng, M.-T. Tseng, W.-Y. Law, C.-J. Kuo, C.-Z. Chiu, C.-M. Chang, S.-H. Lee, H.-M. Lo *et al.*, “Diagnostic performance of 64-versus 256-slice computed tomography coronary angiography compared with conventional coronary angiography in patients with suspected coronary artery disease,” *Acta Cardiologica Sinica*, vol. 29, no. 2, p. 151, 2013.
- [36] Z. Wang, L. Liu, L. Wang, and L. Zhou, “R2gengpt: Radiology report generation with frozen llms,” *Meta-Radiology*, vol. 1, no. 3, p. 100033, 2023.
- [37] X. Zhang, C. Wu, Z. Zhao, W. Lin, Y. Zhang, Y. Wang, and W. Xie, “Pmc-vqa: Visual instruction tuning for medical visual question answering,” *arXiv preprint arXiv:2305.10415*, 2023.
- [38] A. Dosovitskiy, L. Beyer, A. Kolesnikov, D. Weissenborn, X. Zhai, T. Unterthiner, M. Dehghani, M. Mindler, G. Heigold, S. Gelly *et al.*, “An image is worth 16x16 words: Transformers for image recognition at scale,” *arXiv preprint arXiv:2010.11929*, 2020.
- [39] M. D. L. I. Vayá, J. M. Saborit, J. A. Montell, A. Pertusa, A. Bustos, M. Cazorla, J. Galant, X. Barber, D. Orozco-Beltrán, F. García-García *et al.*, “Bimcv covid-19+: a large annotated dataset of rx and ct images from covid-19 patients,” *arXiv preprint arXiv:2006.01174*, 2020.
- [40] K. Papineni, S. Roukos, T. Ward, and W.-J. Zhu, “Bleu: a method for automatic evaluation of machine translation,” in *Proceedings of the 40th annual meeting of the Association for Computational Linguistics*, 2002, pp. 311–318.
- [41] S. Banerjee and A. Lavie, “Meteor: An automatic metric for mt evaluation with improved correlation with human judgments,” in *Proceedings of the acl workshop on intrinsic and extrinsic evaluation measures for machine translation and/or summarization*, 2005, pp. 65–72.
- [42] C.-Y. Lin, “Rouge: A package for automatic evaluation of summaries,” in *Text summarization branches out*, 2004, pp. 74–81.
- [43] R. Vedantam, C. Lawrence Zitnick, and D. Parikh, “Cider: Consensus-based image description evaluation,” in *Proceedings of the IEEE conference on computer vision and pattern recognition*, 2015, pp. 4566–4575.
- [44] T. Dettmers, A. Pagnoni, A. Holtzman, and L. Zettlemoyer, “Qlora: Efficient finetuning of quantized llms,” *Advances in Neural Information Processing Systems*, vol. 36, 2024.
- [45] H. Touvron, L. Martin, K. Stone, P. Albert, A. Almahairi, Y. Babaei, N. Bashlykov, S. Batra, P. Bhargava, S. Bhosale *et al.*, “Llama 2: Open foundation and fine-tuned chat models, 2023,” *URL https://arxiv.org/abs/2307.09288*, 2023.
- [46] A. Q. Jiang, A. Sablayrolles, A. Mensch, C. Bamford, D. S. Chaplot, D. d. I. Casas, F. Bressand, G. Lengyel, G. Lample, L. Saulnier *et al.*, “Mistral 7b,” *arXiv preprint arXiv:2310.06825*, 2023.

- [47] E. J. Hu, P. Wallis, Z. Allen-Zhu, Y. Li, S. Wang, L. Wang, W. Chen *et al.*, “Lora: Low-rank adaptation of large language models,” in *International Conference on Learning Representations*, 2021.

<p>Pneumonia due to colitis. Follow-up. A high-resolution thoracic CT scan is requested. We performed a high-resolution study without contrast. At the current time, marked signs of centrilobular pulmonary emphysema are visualized, predominantly in the posterior segments of the upper pulmonary fields. Two nodular images already present in the previous study are visualized, both subcentimeter: one located at the level of the minor fissure, which represents an intracavitary lymph node, and a second nodular image located in the right upper lobe, practically subpleural in position, without contact with the lower pleura, less than 5 mm, with no changes compared to the previous study. Practically at the current time, no interstitial involvement is visualized that would suggest changes secondary to the current pandemic agent, resolution of the faint ground-glass pattern in a peripheral disposition visualized in the posterior segments of the lower pulmonary fields in the previous study. The rest without changes compared to the previous study.</p>	<p>Clinical judgment: Interstitial pattern under study post-COVID 19 signs of pulmonary hypertension. A thoracic CT scan is requested. High-resolution study performed. Study without contrast. Axial cuts plus sagittal and coronal reconstruction. Marked signs of centrilobular pulmonary emphysema with diffuse predominance in both lung fields, predominantly in the upper lung fields where signs of paraseptal emphysema join. Ascending thoracic aorta caliber 4 cm, pulmonary cone 3.10 cm, no tomographic signs of pulmonary hypertension identified. Mitral valve calcification. Pseudonodular image located at the level of the minor fissure of nonspecific character suggests an intracavitary lymph node. Very faint ground-glass pattern with peripheral distribution in the posterior segments of both lower lobes. Lymph nodes of non-significant size are visualized, arranged at the level of high right paratracheal, paraaortic, low right paratracheal, and subcarinal. No cardiomegaly, no pleural effusion. No bone lesions are visualized.</p>	<p>Chest CT scan exploration. Appearance of extensive right pleural effusion causing complete atelectasis of the right upper lobe and partial of the middle lobe. Notably, there is the appearance of a consolidation in the posterior segment of the right lower lobe with air cavities, likely cavitation vs pneumatoceles, probably attributable to bacterial superinfection. Currently, the opacities of lesser density in the previous study appear as consolidative foci with a reticular aspect on the periphery of the left hemithorax, with an organizing pattern. The pulmonary artery trunk is 32 mm, slightly increased in caliber. No lymph nodes of pathological size or appearance. No other findings to report. Conclusion: Pleural effusion and consolidation in the right lower lobe of new appearance, suggestive of bacterial superinfection.</p>	<p>Plain chest CT technique. Mild intrathoracic goiter, consider requesting an ultrasound to complete the study. No pleural or pericardial effusion observed. No axillary or mediastinal lymphadenopathy. Left axillary lymph node calcified, nonspecific, could be related to a previous granulomatous process, without ruling out other etiologies. To be assessed in the clinical context of the patient. Bilateral pleuroapical fibrotic tracts. Mild cylindrical bronchiectasis in the apical and posterior segments of the upper right lobe, upper left lobe, lingula, associated with mucus plugs and minimal budding tree pattern, without ruling out superinfection. To be correlated clinically and analytically. It could be retractile bronchiectasis secondary to COVID-19 pneumonia in the patient's context or pre-existing, no previous studies available for comparison. Faint patchy mosaic pattern in the lower left lobe that could be residual to COVID-19 pneumonia or secondary to small airway disease. Conclusion: Findings suggestive of small airway disease, with mild bronchiectasis, mucus plugs, and budding tree pattern, without ruling out superinfection. Faint opacities in the lower left lobe that could be secondary to residual COVID-19 pneumonia. Mild intrathoracic goiter, consider ultrasound. See rest.</p>
<p>Urgent pulmonary artery CT scan. Bibasal crackles, decreased vesicular murmur at the right base. Techniques: Angio CT acquisition from pulmonary apices to diaphragmatic domes after intravenous contrast administration. Results: No evident filling defects observed in the main pulmonary arteries, lobar and segmental branches, suggestive of PE (pulmonary embolism). Cardiomegaly. Aortic elongation. No significant alterations in the rest of the mediastinal structures. No mediastinal or axillary lymphadenopathies of significant size observed. Pleural spaces free. Areas of increased ground-glass density, some of nodular morphology, predominantly peripheral in location, affecting all pulmonary lobes, without associated lung consolidations, compatible with moderate to severe COVID-19 infection pneumonia. Conclusion: No evident signs of PE in the examination performed. Radiological signs compatible with pneumonia due to COVID-19 infection, moderate to severe.</p>	<p>Severe subcutaneous and dissecting emphysema of muscular and intermuscular planes, both superficial and deep, at the thoracic level as well as the lower cervical and upper hemiabdomen included in the study. Small right pneumothorax in anteroinferior location. Infiltrates predominantly diffuse bilateral ground-glass with bibasal consolidative areas in the context of known bilateral bronchopneumonia due to COVID-19. Some areas of pulmonary hyperlucency are observed, predominantly in anterior segments and right, attributable to areas of air trapping. No pleural or pericardial effusion is observed.</p>	<p>Technique: thoracoabdominal CT with water as oral contrast and intravenous contrast in the arterial phase, and abdominopelvic in portal and excretory phases. CT scans shows cardiomegaly. Mediastinal spaces are preserved without evidence of lymphadenopathy. No pulmonary nodules are observed. Some small nodular images in both lungs, peripheral, with polyhedral contours, are compatible with intrapulmonary lymph nodes. A mass of approximately 42 mm in diameter, located anteriorly in the interpolar area of the right kidney, which shows contrast uptake but less than the healthy renal parenchyma, heterogeneous, partially occupying the renal sinus and displacing calyces, compatible with renal cell carcinoma as a first possibility, slightly larger in size. Liver, spleen, pancreas, and left kidney are of normal size and morphology, with uniform enhancement density. Adrenals without abnormalities. Simple cyst in the left hepatic lobe and another subcapsular in segment VI. Adequate distribution of mesenteric and retroperitoneal fat planes without evidence of lymphadenopathy or masses. Pelvic varices. Pinching with grade I anterolisthesis of L4 on L5. Right kidney neoplasia without disease extension.</p>	<p>Chronic Lymphocytic leukemia. Suspicion of progression. Thoracoabdominal CT with intravenous contrast. Bilateral axillary lymphadenopathies persist without significant changes, some of large size with preservation of fatty hilum and others oval. Also, bilateral retroperitoneal, mediastinal paratracheal. At the abdominal level, retroperitoneal lymphadenopathies are also maintained at both the interaorticaval and bilateral paraaortic levels, mesenteric, associated with mild panniculitis, as well as in both groins. Thorax: no pleural or pericardial effusion is observed. Hiatal hernia. It has not varied with respect to the previous study. No other pulmonary nodules are observed. Abdomen and pelvis: liver of homogeneous density without evidence of focal lesions. No dilation of the biliary tract is observed. Gallbladder with thin walls without apparent lithiasis or inflammatory changes. Permeable portal vein. Pancreas, spleen, adrenals: degenerative osteodiscal changes in the lumbar spine.</p>

Figure 7: Examples of reports from the BIMCV-RG dataset.

A.4 Data Preprocessing

For each dataset, The Hounsfield Units (HU) of CT scans were clipped to a range of $[-1000\text{HU}, +200\text{HU}]$, reflecting the usable diagnostic range of HU values. Volumes were resized to the following specifications:

1. A resolution of 512×512 on the sagittal and coronal axes, with the transverse axis comprising 256 slices.
2. A resolution of 256×256 on the sagittal and coronal axes, with 128 slices on the transverse axis.

The resized volumes were adjusted to maintain uniform slice spacing of 0.75mm on the sagittal and coronal axes and 1.5mm on the transverse axis. Voxel values across all scans were normalized to a 0 to 1 range. To preserve the integrity of spatial relationships, which is crucial in interpreting 3D medical images, augmentation techniques such as flipping or rotating were not employed. This decision helps avoid potential ambiguities in spatial orientation, such as given radiological reports that specify locations like the ‘left lung’ and ‘right lung.’

A.5 Extra Ablation Studies

Affect of Number of Layers of Projectors We evaluate the effect of varying the number of projectors, \mathcal{F} , from 1 to 3, across two datasets as shown in Fig 8 (left). The results indicate that performance saturates with two-layer projectors and slightly decreases with three layers. Consequently, we select two layers for our model to achieve optimal performance. However, the relatively stable performance across different numbers of layers demonstrates that our method is not sensitive to this factor.

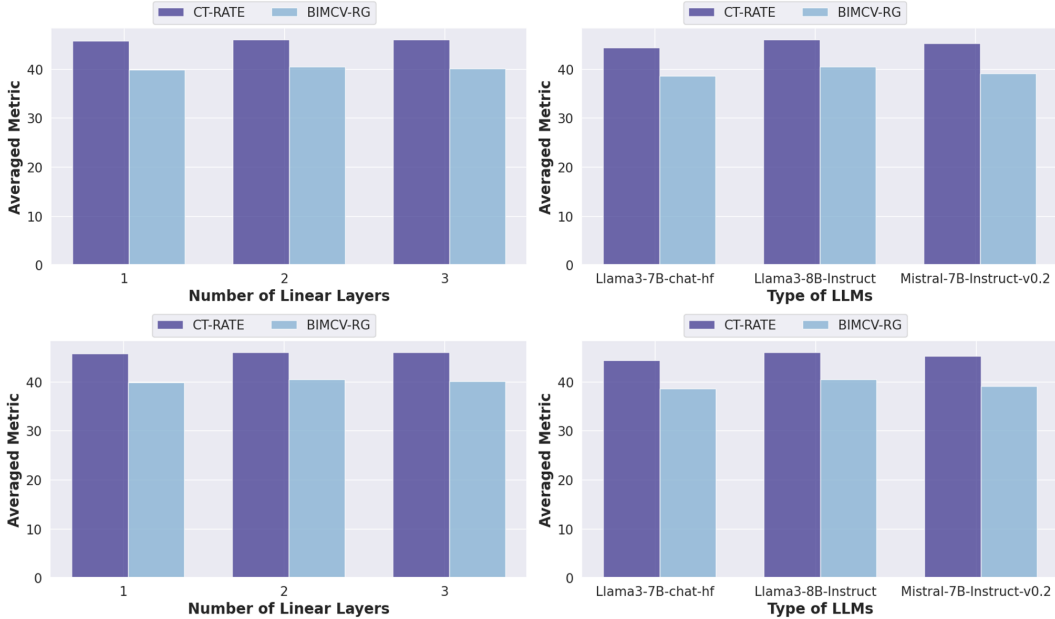


Figure 8: Results from varying numbers of layers in projectors and different LLMs. **Left:** Results from different numbers of layers in projectors applied to both datasets, with an input resolution of $512 \times 512 \times 256$ and using Llama3 as the LLM. **Right:** Results from using different numbers of LLMs on both datasets, each with an input resolution of $512 \times 512 \times 256$.

Table 4: Results of different LR input resolutions are presented. For both LR input resolutions, the HR input resolution is fixed at $512 \times 512 \times 256$. The highest result and the lowest number of visual tokens processed by LLMs are indicated in bold.

LR Input Resolution	Number of Visual Tokens	CT-RATE Averaged Metric	BIMCV-RG Averaged Metric
$128 \times 128 \times 64$	64	46.05	40.96
$256 \times 256 \times 128$	512	46.21	40.85

Effect of Different LLMs We also investigate the impact of different Large Language Models (LLMs) on performance, as depicted in Fig 8 (right), including Llama2-7B-chat-hf [45], Llama3-8B-Instruct [17], and Mistral-7B-Instruct-v0.2 [46]. We achieve optimal performance using Llama3-8B-Instruct, which is currently the most powerful LLM in the 7B-8B scale. This suggests that a stronger foundational LLM leads to better performance in report generation tasks due to enhanced language understanding capabilities. Although Llama3 reaches the highest performance, our method shows minimal fluctuation when LLMs change, indicating robustness across different LLMs.

Effect of LR Input Resolution We explore the effect of two different LR input resolutions, $128 \times 128 \times 64$ and $256 \times 256 \times 128$, to generate LR queries and HILT. For both LR input resolutions, we use the HR input resolution $512 \times 512 \times 256$. As shown in Table 4, a higher LR input resolution leads to an eightfold increase in the number of visual tokens processed by LLMs, indicating a significant increase in computational cost. However, the performance on both datasets does not show the same trend as the computational cost increase. Hence, this suggests that increasing the LR input resolution is not necessary, as we mine HR information from HR views and integrate it into LR queries. Increasing the LR input resolution would not introduce new information but would mainly increase the computational cost.

Table 5: Hyper-parameters for our methods.

Hyperparameters	
Mixed precision	bf16
Instruction tuning epochs	100
LoRA alpha	64
LoRA rank	128
LoRA dropout	0.1
Total batch size	4
Gradient accumulation	2
Maximum sequence length	512
Learning rate	1e-4
Learning rate Optimizer	AdamW
Schedule	linear
Warm-up ratio	0.03
Weight decay	0.0

A.6 Hyper-parameters of Training

In this study, we implement the Low-Rank Adaptation (LoRA) [47] for the 3DHRG task. We configure the LoRA parameters with an alpha of 64 and a rank of 128, and apply a dropout rate of 0.1. Instruction tuning is performed over 100 epochs. All experiments are conducted on a single A100-80G GPU.

For computational efficiency, we employ mixed precision at bf16, as detailed in Tab 5. The training process includes a total batch size of 4 with a gradient accumulation factor of 2, and we restrict the maximum sequence length to 512 tokens.

Regarding learning rates, we use 1×10^{-4} for our models, optimized via the AdamW algorithm. The learning rate schedule is linear with a warm-up ratio of 0.03, and the weight decay is set to 0.0.

We utilize the same configuration for all existing methods if they do not specify these hyperparameters in their official codebase.